Storylines of the 2018 Northern Hemisphere heat wave at pre-industrial and higher global warming levels

Kathrin Wehrli[1], Mathias Hauser[1], and Sonia I. Seneviratne[1]

[1]Institute for Atmospheric and Climate Science, Department of Environmental Systems Science, ETH Zurich, Zurich, Switzerland

Correspondence: Kathrin Wehrli (kathrin.wehrli@env.ethz.ch)

Abstract. Extreme temperatures were experienced over a large part of the Northern Hemisphere during the 2018 boreal summer (hereafter referred to as "NH2018 event"), leading to major impacts to agriculture and society in the affected countries. Previous studies highlighted both the anomalous atmospheric circulation patterns during the event and the background warming due to human greenhouse gas emissions as main drivers for the event. In this study, we present Earth System Model experiments

5   investigating different storylines of the NH2018 event given the same atmospheric circulation and alternative background global warming for: no human imprint, the 2018 conditions, and different mean global warming levels ($1.5°C$, $2°C$, $3°C$, and $4°C$). The results reveal that the human-induced background warming was a strong contributor to the intensity of the NH2018 event, and that resulting extremes under similar atmospheric circulation conditions at higher levels of global warming would reach very dangerous levels. About 32% (61%) of the inhabited or agricultural area in the investigated region would reach

10   maximum temperatures over $40°C$ under $2°C$ ($4°C$) of global warming and similar atmospheric circulation conditions.

1 Introduction

During the 2018 boreal summer, large parts of the Northern Hemisphere experienced extreme temperatures, leading to major impacts to agriculture and society in the affected countries (Vogel et al., 2019). The event (hereafter referred to as "NH2018

15   event") was associated with near-simultaneous heat waves on three continents, including North America, Western and Northern Europe, as well as Japan (Kornhuber et al., 2019b; Vogel et al., 2019). Previous studies highlighted both the anomalous atmospheric circulation patterns during the event and the background warming due to human greenhouse gas emissions as main drivers for the event (Drouard et al., 2019; Kornhuber et al., 2019b; Toreti et al., 2019; Vogel et al., 2019). The NH2018 event was characterized by a hemisphere-wide wavenumber 7 circulation pattern, which was also observed during the European heat

20   waves of 2003, 2006 and 2015 (Kornhuber et al., 2019b). A strong positive mode of the North Atlantic Oscillation contributed significantly to the extreme summer conditions in Europe by amplifying the weather anomalies induced by the wavenumber 7 pattern (Drouard et al., 2019). An analysis of simulations from the 5th phase of the Coupled Model Intercomparison Project

(CMIP5, Taylor et al., 2012) showed that the total area affected by hot extremes during the NH2018 event, despite being un-
precedented in the historical record, was actually consistent with the present-day level of global warming (Vogel et al., 2019).

25 Indeed, it had approximately a 16% probability of occurrence under present global warming in the CMIP5 simulations (Vogel
et al., 2019). However, no studies were conducted so far to disentangle the contribution of the anomalous circulation patterns
vs. background global warming for the climate anomalies during the NH2018 event.

In this study, we present numerical experiments investigating different storylines of the NH2018 event given alternative
background global warming but the same atmospheric circulation anomalies. While it cannot provide information on proba-

30 bility, the storyline approach allows to explore uncertainty of future climate and the consequences of a specific event in order
to improve understanding of the driving factors involved (Hazeleger et al., 2015; Shepherd et al., 2018). The alternative back-
ground global warming conditions applied in the experiments include: a) no human imprint (i.e. natural/ pre-industrial climate
conditions), b) 2018 conditions (corresponds to approximately $1.1°C$ of global warming in the CMIP5 multi-model mean), c)
$1.5°C$, d) $2°C$, e) $3°C$ and, f) $4°C$ of global warming. The atmospheric circulation in the experiments is nudged to the observed

35 wind patterns during the NH2018 event following the approach of Wehrli et al. (2019). Hence, all of the experiments include
the same circulation patterns but different background global warming. These experiments are of particular relevance since
events associated with the type of circulation patterns from the NH2018 events could lead to high risks of crop failures across
several breadbasket regions of the world (Kornhuber et al., 2019a).

2 Model and methods

40 Global climate model simulations are conducted with the Community Earth System Model version 1.2 (CESM, Hurrell et al.,
2013). Historical sea surface temperatures (SSTs) and sea ice fractions are prescribed using transient monthly observations
from a merged product combining the Hadley Centre sea ice and SST data set, version 1 (HadISST1) up to 1981 with the
weekly optimum interpolation SST analysis version 2 by the National Oceanic and Atmospheric Administration (NOAA
OIv2) thereafter (Hurrell et al., 2008). We produce SSTs and sea ice consistent with the different background climates as

45 described in Sect. 2.4 and Sect. 2.5. To simulate the Earth's atmosphere, CESM utilizes the Community Atmosphere Model
version 5.3 (CAM5, Neale et al., 2012). Here we couple CAM5 to a nudging module to control the atmospheric circulation
as described in Sect. 2.2. For the representation of land surface processes, CESM uses the Community Land Model version 4
(CLM4, Lawrence et al., 2011; Oleson et al., 2010). CAM5 and CLM4 are both run on $0.9°$ x $1.25°$ horizontal resolution with
30 layers up to $2\,\mathrm{hPa}$ for the atmospheric component (CAM5) and 10 hydrologically-active soil layers down to $3.8\,\mathrm{m}$ for the

50 land component (CLM4). Solar forcing follows the model default historical data until the end of 2005 and historical and future
simulations of the forcing compiled for CMIP6 thereafter, as in Wehrli et al. (2019) (see Matthes et al., 2017, for solar forcing).
Aerosols and land use/ vegetation follow CMIP5 recommendations for the 20th century simulation until the end of 2005 and
the representative concentration pathway 8.5 thereafter (RCP8.5, van Vuuren et al., 2011). Likewise, greenhouse gases (GHGs)
follow CMIP5 historical recommendations and then after 2006 they are prescribed from observations for CO_2, CH_4, N_2O, and

55 RCP8.5 for other GHGs. Observed global means of CO_2, CH_4, and N_2O were obtained from NOAA (CO_2: Dlugokencky and

Table 1. Overview of simulations

Name	Year	Atmospheric forcing	CMIP5 MMM warming [$^{\circ}$C]	Actual warming [$^{\circ}$C]
climatology	1981–2010	historical+RCP8.5	–	–
historical	2018	historical+RCP8.5	1.12	1.24
natural	2018	pre-industrial+historical	0.0	0.0
warming15	2028	RCP8.5	1.5	1.60
warming20	2042	RCP8.5	2.0	2.18
warming30	2064	RCP8.5	3.0	3.27
warming40	2085	RCP8.5	4.0	4.39

Year corresponds to the year analysed in this study and atmospheric forcing refers to the solar, aerosol, and greenhouse gas forcing. The warming given is relative to a pre-industrial time period (1861–1880) and corresponds to the CMIP5 multi-model-mean (MMM) warming for the respective simulation years. Per design the temperature for the natural simulation is set as reference for 0 global warming. The actual warming in the CESM simulations differs from the CMIP5 MMM.

Tans, 2019; CH$_4$: Dlugokencky, 2019; and N$_2$O: NOAA Earth System Research Laboratory, 2019).

Each experiment is run for four years; the first three years (2015–2017) are used as spin-up, and 2018 is analysed. A climatology for the historical simulations is obtained from a longer simulation that covers the years 1981–2010.

60 ## 2.1 Natural and warming scenarios

The NH2018 event serves as a reference to investigate its resulting characteristics in hypothetical conditions, or storylines, with the same atmospheric circulation but different levels of global warming. In addition to the historical simulation we run one simulation with pre-industrial-like conditions ("natural") and four simulations that follow global warming scenarios. An overview is given in Table 1. For the natural simulation volcanic aerosols and solar radiation are set to historical conditions,

65 whereas we use pre-industrial GHGs, aerosols and SSTs (Sect. 2.4). The four warming scenarios are designed to match 1.5°C, 2°C, 3°C and 4°C global mean warming with respect to pre-industrial conditions (1861–1880) of the CMIP5 multi-model-mean (MMM). We will hereafter refer to these experiments as warming15, warming20, warming30 and warming40. Aerosols, GHGs and SSTs follow RCP8.5. The actual warming of the scenarios slightly differs from the target values, which will be discussed in Sect. 4. All simulations are nudged towards 2015–2018 atmospheric circulation (1981–2010 for the climatology).

70 ## 2.2 Nudging of the atmospheric circulation

To impose the large-scale circulation of the event year (2018) in the model, we use atmospheric nudging of the horizontal winds. The approach is described and validated in Wehrli et al. (2018) and Wehrli et al. (2019). The horizontal winds are relaxed toward observations using a height-dependent nudging function (for the profile see Wehrli et al., 2018). At the surface

the nudging strength is set to zero, meaning that the land surface can interact with the atmosphere through surface turbulent

75 fluxes, resulting in balanced surface climate and winds. The large-scale circulation (mostly above 700 hPa) is forced to follow the observations and thus ensures that the observed large-scale weather patterns are reproduced (see Kooperman et al., 2012; Wehrli et al., 2018; Zhang et al., 2014). As a proxy for the observed winds, we use zonal and meridional 6-hourly wind fields from the ERA-Interim reanalysis (Dee et al., 2011). The nudging of the circulation ends on July 27th 2018 due to availability of the input fields.

2.3 Determination of warming levels in CMIP5

To produce the ocean fields for the natural and warming scenarios we use model output from the historical and RCP8.5 emissions scenarios from the CMIP5 data archive. We use one simulation per model ("r1i1p1"). To find the years corresponding to the chosen warming scenarios in the CMIP5 ensemble we use near-surface air temperature ("tas"). The pre-industrial reference period is given as 1861–1880. Warming levels with respect to pre-industrial are then determined by taking the difference

85 between annual global mean temperature from RCP8.5 and pre-industrial for each model individually. A 21-year centred running mean is applied to the differences and we then compute the MMM. Following this approach, we obtain a CMIP5 MMM warming of $1.12°C$ for 2018. The $1.5°C$, $2°C$, $3°C$ and $4°C$ MMM warming levels are reached in 2028, 2042, 2064, 2085, respectively.

2.4 Sea surface temperatures representative of prescribed warming levels

90 To derive SSTs consistent with the different background climates we add delta SST fields to the observed monthly SSTs. The delta SST fields are computed from the CMIP5 SST fields ("tos"), which were regridded to a common grid of $1° \times 1°$. We first apply a 21-year running mean over the monthly merged historical + RCP8.5 tos data and then average over the models. Using these temporally-smoothed monthly fields between 1979–2020 and for 2028, 2042, 2064 and 2085, as well as the monthly climatology of the pre-industrial tos fields we compute the transient delta SSTs by taking the differences. These delta SSTs

95 (see also Fig. 2) are then added to the NOAA OIv2 historical data to create the SSTs that are prescribed in our scenarios. The detailed step-by-step procedure is given in the Appendix (B1).

2.5 Generation and prescription of sea ice

Although it would be possible derive a delta field for sea ice similarly to the SSTs, this would result in a sea ice field that is not in balance with the new SSTs. Therefore, we derive a relationship between sea ice fraction anomalies and SST anomalies with

100 respect to a climatology, similarly as in the "Half a degree additional warming, prognosis and projected impacts" experiments (HAPPI; Mitchell et al., 2017). Monthly SST and sea ice anomalies are computed for the years 1996–2015 from the climatology of the same years, using ocean observations from NOAA OIv2. A linear regression is then fitted to the anomalies for each month-of-the-year, longitude and for both hemispheres separately. The slope and intercept are smoothed zonally first, before they are then used to compute sea ice anomalies for the natural and warming scenarios as a function of the delta SST field.

As an extension of the method applied in the HAPPI experiments we only consider grid cells that undergo a change of sea ice fraction of over 50% for the month in consideration. This ensures that grid cells that are not experiencing enough variability during 1996–2015 are excluded from the analysis. For example, a grid cell close to the north pole may always have a sea ice fraction larger than 90% while the ocean temperature usually does not change at all and does therefore not allow for a robust estimation of the slope and intercept. Consequently, the given grid cell would not melt even under very high global warming.

To compute the regression of a grid cell we pool SST and sea ice anomalies of all valid grid cells that are within three grid cells to the west and to the east and along the meridian in the same hemisphere. Should no valid grid cells be in this area, more grid cells in the longitudinal direction are included gradually (extending box approach). The slope and intercept from this regression are smoothed along the longitude using a 500 km smoother as is done for HAPPI. We further tested an approach where not all grid cells along a meridian were included, but up to two grid cells to the north, south, east, and west of a specific grid cell (5 x 5 grid cells in total). The results are very similar to the first method (not shown). We choose the first method because the resulting sea ice field is overall smoother. The new set of SSTs and sea ice for each scenario is adjusted according to the constraint of Hurrell et al. (2008), which ensures that (i) sea ice fraction is 100% at $-1.8°$C, and SSTs do not get colder than that, (ii) there is no sea ice at water temperatures warmer than $4.97°$C, and (iii) that within this temperature range the maximum sea ice fraction is limited by a temperature-dependent function.

We contrast our method to the one developed for the "Climate of the 20th Century Plus Detection and Attribution" project (C20C+DA; Stone et al., 2019). For this method, a linear relationship is determined using absolute values of SST and ice coverage instead of anomalies. The regression is calculated by pooling all ice-covered grid cells of the Northern and Southern Hemisphere, respectively. Ice coverage is binned in 100 equally-sized bins and the median SST for each ice bin is determined. The line through the centre of mass of all the bin medians is then estimated by a linear fit. This method was developed to compute sea ice estimates for natural historical simulations (i.e. a cooling). Therefore, it comes with an algorithm that prevents ice from melting and only adds new ice where SSTs cool. As we require a method that works for positive and negative delta SSTs we do not implement the full algorithm but only make use of the linear relationship. For 20C+DA the years 2001–2010 were used to determine the relationship. For consistency we take the years 1996–2015. Again, we apply the constraint of Hurrell et al. (2008). We hereafter refer to this method as SP equation.

2.6 Data sets and data analysis

The atmospheric nudging uses ERA-Interim 6-hourly horizontal wind fields. Mean daily near-surface temperature fields are retrieved from ERA-Interim for comparison to our results. Observed daily maximum near-surface temperatures (TX) are obtained from ERA-Interim and Berkeley Earth (Rohde et al., 2013a, b). Mean daily temperature, TX and precipitation are retrieved from the Modern-Era Retrospective analysis for Research and Applications, Version 2 (MERRA-2, Gelaro et al., 2017). The observations/ reanalysis data is remapped to the resolution of CESM using second-order conservative remapping (Jones, 1999). Results are shown for the absolute values of the variables as well as for anomalies with respect to the 1981–2010 climatology.
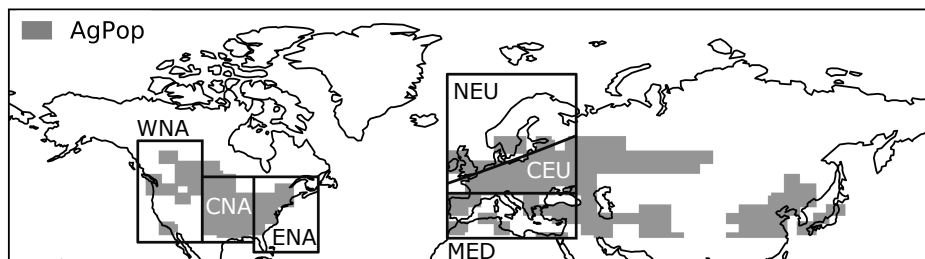
Figure 1. Study regions. Shown by the grey shading are regions north of $30°$N with high population density and/ or high importance for agriculture (AgPop). The black outlines mark the location of selected SREX regions in America and Europe.

2.7 Study regions

We show results only north of $25°$N. For regional averages we choose the regions defined in the IPCC Special Report on Managing the Risks of Extreme Events and Disasters to Advance Climate Change Adaptation (SREX; Seneviratne et al.,
140 2012). We show results for the European and American regions as highlighted in Fig. 1. In addition, we focus on a region north of $30°$N that is especially vulnerable to extreme conditions because it is either densely populated (more than 30 km^{-2}) and/ or an important area for agriculture. We define this "human-affected and human-affecting" region following Seneviratne et al. (2018) and Vogel et al. (2019) and refer to it as AgPop (see Fig. 1).

3 Results and discussion

145 We first evaluate the sea ice reconstruction method introduced in this study against observed sea ice and compare the performance to the SP equation in Sect. 3.1. Then we present the results for the natural and warming scenarios in Sect. 3.2 and discuss their implications for possible future events. In Sect. 3.3 we discuss how TX scales with an increase in global mean temperature and if the NH2018 atmospheric circulation influences this relationship.

3.1 Evaluation of sea ice reconstruction

150 Historical sea ice fields are computed using the methods described in Sect. 2.5 and evaluated against NOAA OIv2 ice (see Appendix Fig. A1). While the method using the SP equation generally overestimates sea ice, over- and underestimation nearly balance out when taking a time average over multiple years for the method presented here. Hence, the root mean squared error (RSME) for ice grid cells is $< 1\%$ using the new method while it is around 5% using the SP equation. For a single year the errors are larger, 5.6% and 8.5% for the year 2018 for the new method and SP, respectively. It is not possible to evaluate the
155 performance of the sea ice reconstruction for the natural and warming scenarios. The two methods suggest a change of $+10\%$ to $+14\%$ in the annual mean with respect to currently observed sea ice fraction for the natural scenario, -4% to -7% for the $2°$C warming scenario and -26% to -27% for $4°$C warming (Fig. 2, see Appendix Fig. A2 for the absolute ice fields for
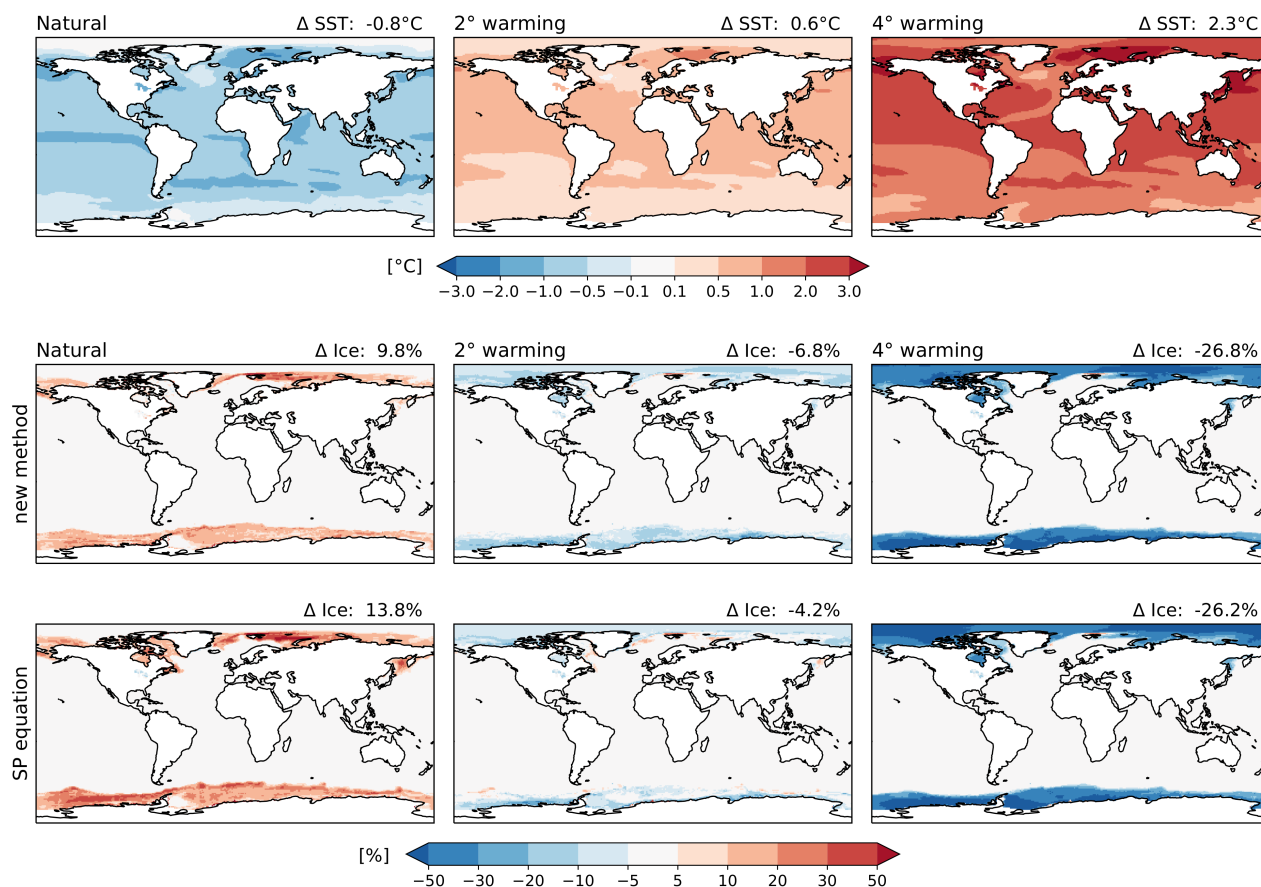
Figure 2. Change in SST and sea ice coverage with respect to historical conditions from NOAA OIv2 for the natural (left), warming20 (middle) and warming40 (right) scenarios. (top row) Average delta SST for 2018 under the three climate scenarios. (centre row) Average sea ice coverage change for 2018 under the three climate scenarios using the sea ice estimation method developed in this study. (bottom row) same as in the centre row but using the SP equation to compute the change.

the new method). Note that the two methods show larger differences for the natural scenario but agree more for the warming scenarios.

3.2 Storylines for the NH2018 event

During late June and the first weeks of July 2018 an exceptionally strong and persistent Rossby wavenumber 7 pattern dominated the weather in the Northern Hemisphere (Drouard et al., 2019; Kornhuber et al., 2019b). The wave pattern was associated with simultaneous extreme events across the entire hemisphere including heat waves in the western United States, eastern Canada, western Asia and large areas in Europe (Kornhuber et al., 2019b; NOAA, 2018; Vogel et al., 2019). In Europe, the July temperature anomaly was ranked second highest on record, just one hundredth degree Celsius behind 2015 (NOAA,

2018). Vogel et al. (2019) show that the area of important "human-affected and human-affecting" regions (AgPop) experiencing simultaneous heat waves peaked at the end of July. Hence, we focus here on the month of July 2018 and especially on a 15-day period at the end of the month from July 13 to 27 (which also corresponds to the last days of our simulations where the atmospheric nudging is available).

170   Comparison of the temperature anomaly to ERA-Interim shows that the daily and 15-day mean anomalies are well represented in the nudged historical CESM simulation (Fig. 3). Similar results are obtained for MERRA-2 (not shown). For 13 to 27 July 2018 the mean daily temperature in the historical simulation is on average 5°C warmer than the climatology (1981–2010) for large areas in Scandinavia and some smaller areas in Germany, Belgium and the Netherlands (maps in Fig. 3). In Northern America temperatures are 2.5 to 5°C above average for Neufundland, Québec, Texas and northern Mexico as well as most

175 of the Western North American (WNA) region. An intensification of the hot anomaly can be seen for the Central European (CEU) and Northern European (NEU) regions during July, whereas in the AgPop region the anomaly is around 1.5 to 2°C for the entire month (time series plots in Fig. 3). TX over the same time period is even more than 7.5°C warmer than the climatology in much of Scandinavia and Northern Germany, Belgium and the Netherlands (Fig. 4 and Appendix Fig. A3 for comparison to ERA-Interim, MERRA-2 and Berkeley). In contrast, TX for much of the Mediterranean (MED) region is close

180 to the climatological average. Colder-than-average TX is seen for areas surrounding the Aegean Sea and Black Sea, as well as for Portugal, parts of Spain and for the United States east coast (Fig. 4). The temporal evolution of the TX anomaly during the month of July resembles that of the daily mean temperature (Appendix Fig. A4).

     In the nudged historical simulation maximum daytime temperatures (TXx) exceeding 40°C are simulated for parts of the Central North American (CNA) region and for a few locations in northern France, Belgium and the Netherlands. The fraction

185 of the AgPop region affected by TXx > 40°C is 20%. In the natural scenario mean TX anomalies exceed 7.5°C virtually nowhere (except for five grid cells) in the entire Northern Hemisphere north of 25°N (Fig. 4). TXx during 13 to 27 July does not exceed 40°C for the European regions and only 12% of the AgPop region is affected by such high temperatures. Although the circulation pattern induces anomalous temperatures in the same regions as in the historical case, very extreme temperatures > 40°C are confined to areas that climatologically have higher likelihood to experience hot temperatures such as northern

190 Africa. On the other hand, the warming scenarios show an extreme intensification of the magnitude and extent of the event. In the warming20 scenario the fraction of the AgPop region experiencing > 40°C temperatures increases to nearly one third of the total area and it almost doubles to 61% for the warming40 scenario. At 4°C global warming the model predicts that most of the United States will experience temperatures above > 40°C given the 2018 circulation pattern (Fig. 4). For much of CNA anomalies with respect to 1981–2010 exceed 10°C. Large areas of CEU and NEU experience temperatures around 38°C and

195 higher, which corresponds to more than 10°C above climatology for Scandinavia.

     The NH2018 event did not only bring exceptionally warm temperatures to central and north-western Europe but also a dry spring and summer contributed to severe drought conditions (Toreti et al., 2019). In contrast, south-eastern Europe experienced a wetter-than-usual spring and summer (Toreti et al., 2019). This marked precipitation dipole over Europe is reproduced in the historical simulation (Fig. 5). In addition, over North America a contrasting precipitation pattern can be found with a strong

200 positive anomaly in the east and a precipitation deficit in the west (Fig. 5). In the warming40 scenario we find a decrease of up
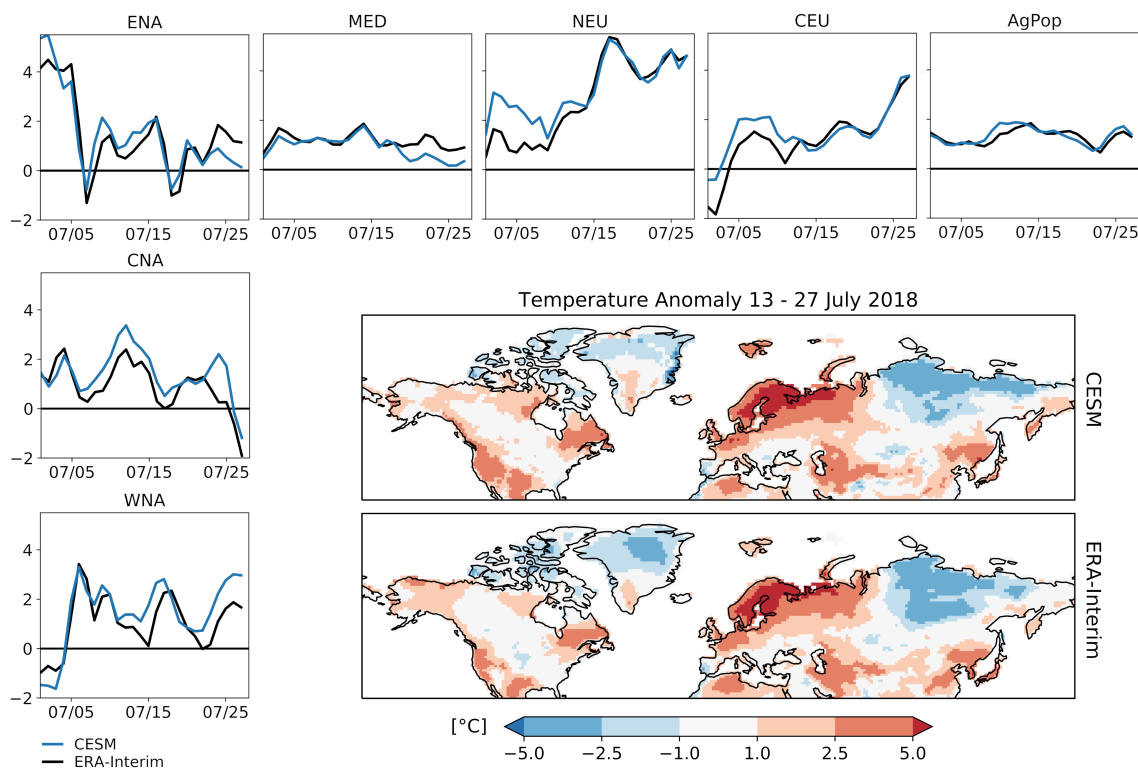
Figure 3. Anomalies of mean daily temperature with respect to the 1981–2010 climatology. The maps show the average anomaly over 13 to 27 July 2018 for the nudged historical CESM simulation (top) and for ERA-Interim (bottom). The time series show the daily temperature anomaly for CESM (blue) and ERA-Interim (grey) for the month of July averaged over six SREX regions as well as for the AgPop region.

to -60% in precipitation over Mediterranean Europe and CNA compared to the historical simulation (Fig. 6, left). For Europe these changes in precipitation counteract the precipitation dipole observed in the historical simulations but precipitation still remains above climatology for most of Mediterranean Europe. Over a smaller region in CNA there is already a precipitation decrease of around 40% in the warming20 scenario. The precipitation decrease co-occurs with a decrease of up to 25% in total

205   cloud cover fraction for central North America in the warming40 scenario (not shown) as well as higher net shortwave radiation at the surface for large parts of North America and Europe (Fig. 6, right). Further, the increase in net shortwave radiation goes along with a decrease in latent heat flux and an increase in sensible heat flux, which is most pronounced in the warming40 scenario for CNA and central Europe (not shown). This change in the surface fluxes implies a reduction in evaporative cooling and increase of near-surface heating, which can amplify the heat wave (Fischer et al., 2007; Seneviratne et al., 2006, 2010).

210   Hence, in a warmer climate the heat wave during a NH2018-like event might be amplified through land-surface feedback. Further, some of the regions experiencing precipitation excess might be seeing less precipitation. This agrees with findings by Toreti et al. (2019) showing that the projected likelihood of anomalously wet conditions as observed during NH2018 decreases for southern Europe. On the other hand, in the natural scenario the event is less extreme due to higher total cloud cover (not
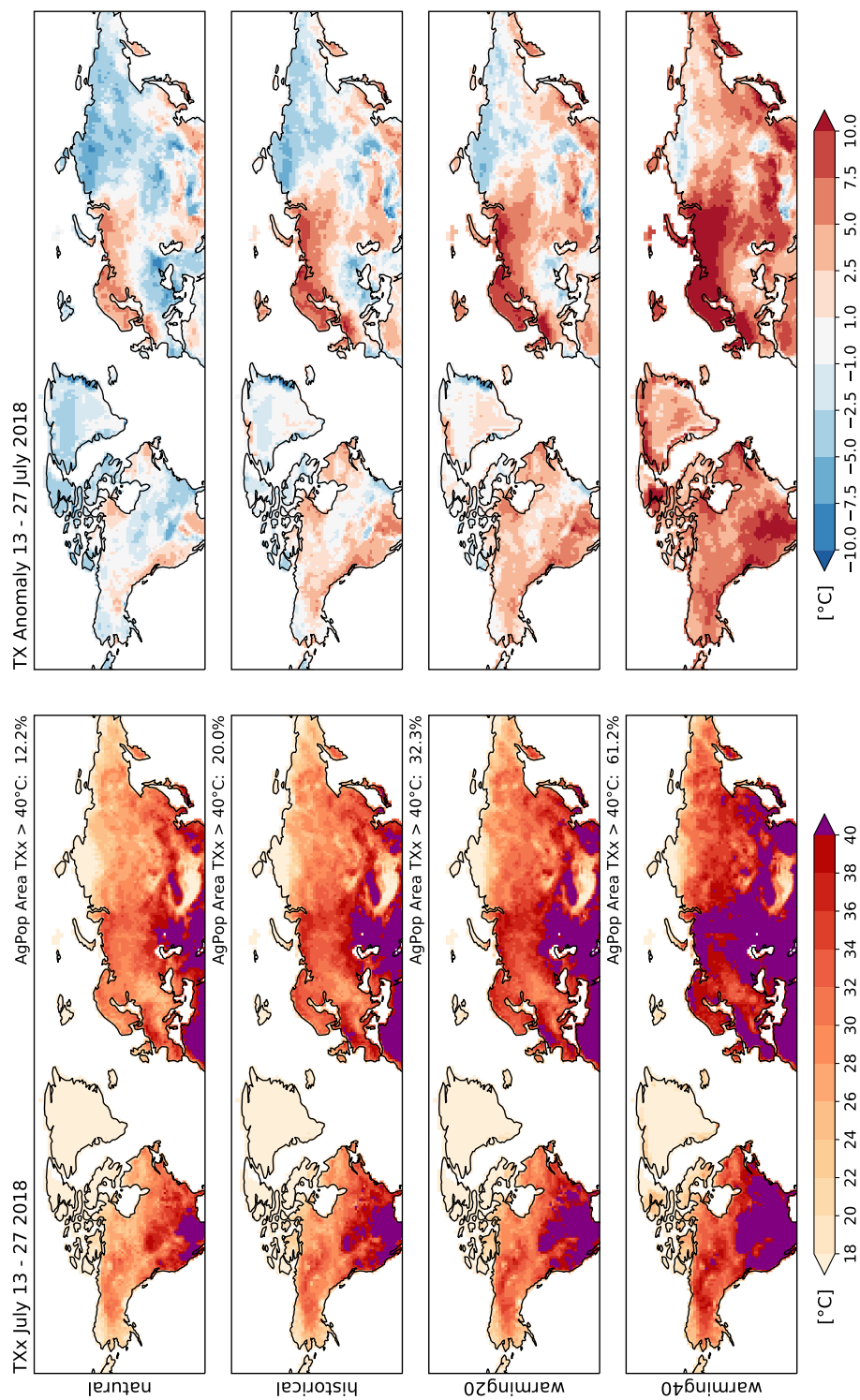
Figure 4. Daily maximum temperature (TX) for July 13 to 27 2018. (left) Maximum TX (TXx) over the 15-day period. The model simulations were corrected by the mean (1981–2010) climatological TX bias compared to Berkeley-Earth. The number in the upper right corner indicates the fraction of the AgPop area where temperatures exceed 40°C. (right) Anomaly of mean TX over the 15-day period compared to the 1981–2010 historical climatology (uncorrected).
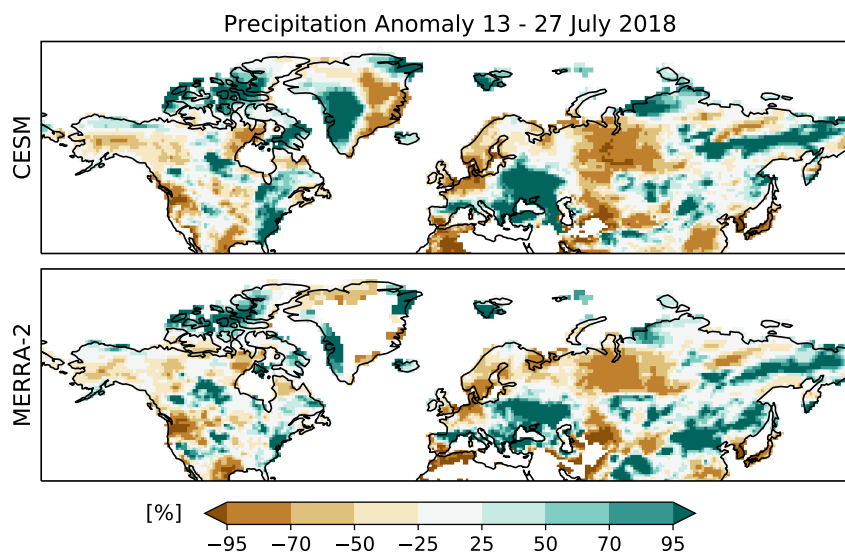
Figure 5. Precipitation Anomaly (%) for July 13 to 27 2018 compared to 1981–2010 climatology. (top) CESM historical simulation (bottom) MERRA-2. Areas with less than 0.1mm/day precipitation in the climatology are masked out.

shown), less net shortwave radiation (Fig. 6, right), an increase of precipitation, especially for CNA (Fig. 6, left), and higher

215 soil moisture (not shown). Together with the colder background climate these effects combine to reduce the maximum reached temperatures and abate the heat stress for example for crops. In short, we find that the NH2018 event would have been less widespread and less hot under natural climate conditions. Contrarily, it would have affected an even much larger area and would have caused particularly dangerously high temperatures and severe drought conditions in a large fraction of the AgPop region under higher levels of global warming.

220 **3.3 Scaling of local temperature increase with global warming**

We scale the increase in July mean TX of each study region with the global mean temperature change in our scenarios. As our simulations are all nudged toward the 2018 atmospheric circulation, we compare the results to simulations with random circulation from CMIP5 and in specific to the CESM simulations in CMIP5 (CMIP5-CESM). This way it is possible to disentangle the effect of the specific circulation pattern from the global mean warming trend qualitatively (note, however, that CMIP5-

225 CESM uses an interactive ocean). The simulation years from the CMIP5 models are chosen to equal the actual warming for the CESM simulations (Table 1). In general, the increase in TX with global mean warming between $1.2°C$ and $4.4°C$ follows a linear relationship (Fig. 7). For MED both CESM simulations as well as the CMIP5 MMM lie close together and there is little spread between the CMIP5 models (orange shading). This indicates that the CESM model behaves similarly to the CMIP5 MMM and that there is no change in the relationship induced by the atmospheric circulation of 2018. Hence, the increase in

230 TX is driven by the background global warming. For WNA and CEU both CESM model configurations simulate a higher TX
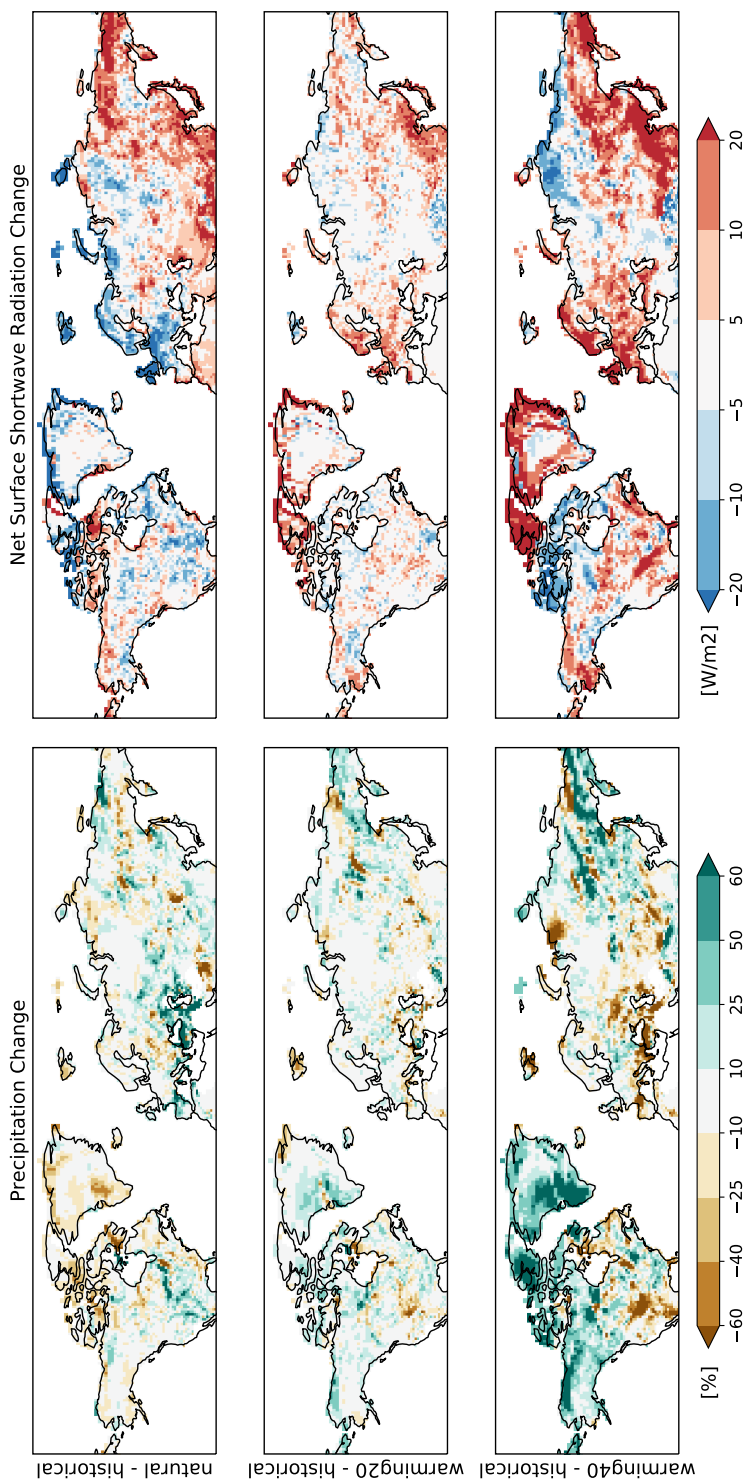
Figure 6. Changes in precipitation (left, %) and net shortwave radiation at the surface (right, W/m2). Changes are averaged over 13–27 July 2018 and are given as anomalies from the historical simulation. Areas with less than 0.1 mm/day precipitation in the historical simulation are masked out in the left plot.

for a given warming level than the CMIP5 MMM, indicating that CESM produces warmer future climate in general for these regions. However, the nudged CESM simulations show a very similar increase of TX as CMIP5-CESM, which implies that for these regional averages the 2018 circulation did not alter the relationship to the global mean temperature. Both SREX regions cover a rather large and climatologically diverse area. In the nudged historical simulation positive TX anomalies are observed in the western part of the CEU region and negative anomalies in the east (Fig. 4). The two circulation-related contributions likely compensate each other when computing the regional average for the historical simulation and also for the warming scenarios, which might be the reason why the scaling is similar to the non-nudged simulations. For NEU, CNA and Eastern North America (ENA) TX from the nudged CESM model shows different behaviour from CMIP5 and CMIP5-CESM, whereas the latter two behave rather similarly. TX from the nudged simulations shows a steeper increase with global warming compared to the CMIP5 models and even exceeds the envelope of CMIP5 models at the highest level of global warming ($4.39°$C). Hence, there is an effect of the circulation pattern in these regions which linearly increases for the same event at higher global warming levels. For ENA TX is mostly around climatological values or even below in the historical simulation. Therefore, it is counter-intuitive that for the warming scenarios TX increases due to the same circulation pattern. We speculate that this is related to the increase in shortwave radiation seen for ENA at higher global warming scenarios such as warming40 (Fig. 6). For CNA there is a steeper increase of TX between the $2.18°$C and $3.27°$C global mean warming which might be related to a change in surface heat fluxes and stronger land-atmosphere coupling as was found in Sect. 3.2. The AgPop region spans across several of the SREX regions evaluated here, mainly CNA, CEU and MED. Therefore, the relationship is a combination of the effects described above. For the relationship between July mean temperature and global warming the results look similar except for the AgPop region where the differences between the nudged CESM and CMIP5-CESM disappear (not shown).

4 Conclusions

We present an analysis of scenario storylines building on the extreme 2018 Northern Hemisphere summer ("NH2018 event"). These storylines retell the NH2018 event in alternative worlds with the same atmospheric circulation as observed but different background global mean warming (and associated sea ice cover). The event is alternatively simulated in a natural setting without human imprint on the climate system ("natural"), for the present-day climate conditions, and for four scenarios at different levels of global warming ($1.5°$C, $2°$C, $3°$C, and $4°$C). All simulations nudge the large-scale atmospheric circulation toward the 2018 conditions but differ in their greenhouse gas and aerosol forcing as well as in the SSTs and sea ice coverage of the ocean. These storylines for the NH2018 event show drastic consequences for the entire Northern Hemisphere in case of a re-occurrence of this atmospheric pattern at higher global warming. Maximum temperatures increasingly surpass $40°$C with large parts of the United States experiencing such extreme temperatures already at $2°$C global warming. At $4°$C almost the entire United States as well as large areas of Western Europe and Asia are affected by such extreme temperatures. The total area of important "human-affecting and human-affected" regions (Seneviratne et al., 2018; Vogel et al., 2019) in the Northern Hemisphere (north of $30°$N) experiencing temperatures higher than $40°$C increases from 20% during the NH2018 event to 32% and 61% at a global warming of $2°$C and $4°$C, respectively. We find that TX for the different scenarios linearly increases
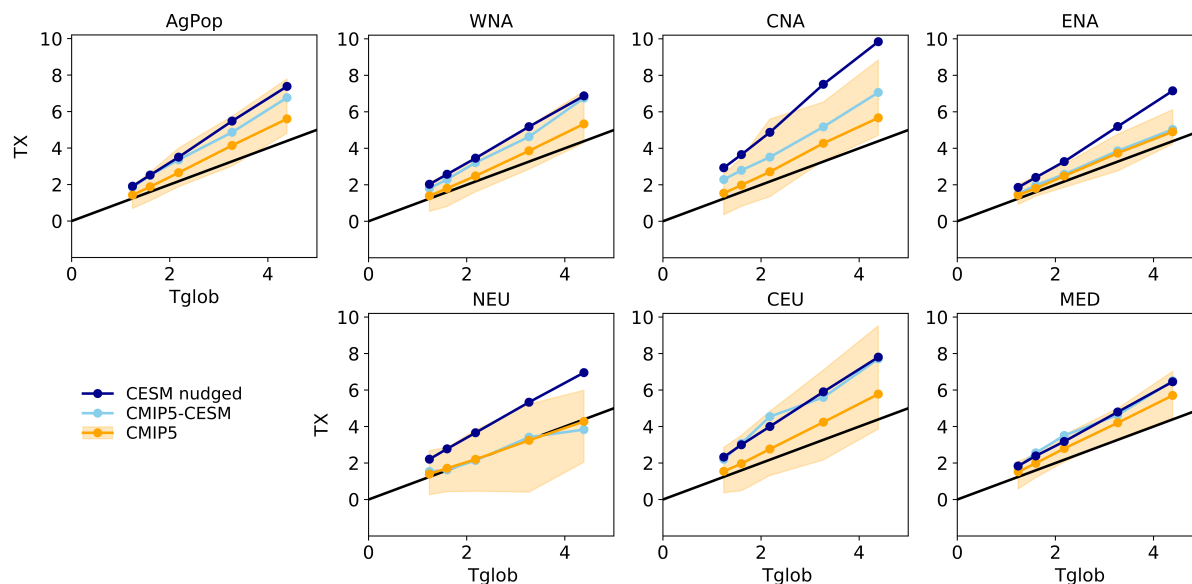
Figure 7. Scaling of daily maximum temperature (TX) for July with global mean warming (Tglob) for the study regions. Shown is the July mean temperature from the nudged CESM simulations (dark blue; until July 27), the CMIP5 multi-model-mean (orange line) and the full model range (orange shading) as well as for CESM from the CMIP5 ensemble (CMIP5-CESM, light blue) separately. The black line indicates the 1:1 line.

with global mean warming. For the CNA, NEU and ENA region we find a steeper slope of the relationship, indicating that
these regions are affected by an amplification of the heat wave in a warming climate. However, it is important to keep in mind
that even if the increase in temperature is linear, the associated impacts would likely not be. Human well-being, crop yields
and fire risk for example are related to certain temperature ranges and effects of the heat wave might be amplified once certain
thresholds are surpassed. In the "natural" simulation, temperatures remain below $40°C$ for most regions north of $30°N$ and
stress on plants is further reduced by higher precipitation and soil moisture in the natural climate conditions.

It is intrinsic to this kind of simulations that there is no atmospheric variability among ensemble members, which prevents
an assessment of the probability of the scenarios. The study is thus not designed to answer the question of how probable it is for
a NH2018-like event to re-occur at a certain warming level. Statistically the probability that exactly the same circulation with
the same history and evolution during the heat wave will re-occur is small. Further, the nudging approach does not ensure that
the circulation pattern is physically in balance with the scenarios for higher global warming or natural conditions. Hence, it
might be that it is unlikely that the atmospheric circulation patterns associated with NH2018 event could establish in a warmer
climate, which we cannot assess in this kind of study. However, it has been shown from observations that the occurrence
of the driving NH2018 atmospheric circulation pattern, a stationary wavenumber 7 Rossby wave, has increased significantly
in recent years, a possible consequence of the enhanced land-ocean temperature contrast due to global warming (Kornhuber

et al., 2019b). Even if there should be no trend in amplitude or persistence of these wave events, associated heat waves in a
280   future climate will be amplified by the global warming (Kornhuber et al., 2019a). From a dynamical perspective, it appears
thus probable that similar wave events will occur in a warmer climate and thus the study of such hypothetical events is highly
relevant.

      The warming levels and corresponding atmospheric forcing were chosen based on the global mean warming using near-
surface air temperature of the CMIP5 MMM and from this corresponding delta SSTs were computed. However, this does
285   not imply that the same warming levels will be reached in our model. Indeed, the global mean warming in the simulations is
higher. It was shown that computing blended global mean temperature from near-surface air temperature and SSTs together
with accounting for incomplete data from observations leads to approximately $0.2°C$ less global warming since the 19th century
(Cowtan et al., 2015; Richardson et al., 2016). Applying this to our simulations the discrepancy between the target warming
level and actual warming is reduced. Still, to simulate the target warming with better accuracy a workaround could be to
290   choose the years corresponding to a target warming level from CESM itself (using blended global mean temperatures) and also
computing the delta SSTs only from CESM (by using the CESM model data from CMIP5 or by running a long, non-nudged
simulation with prescribed ocean following e.g. RCP8.5 scenario). We argue that even if the target warming might be simulated
with better accuracy, the results would not differ fundamentally from those found here as we show that local temperatures in
the simulations scale approximately linearly with global warming.

295   To our knowledge this is the first study to use storylines of different warming levels for a specific event in a global climate
model setup. Kornhuber et al. (2019a) show that in the future the wavenumber 7 circulation pattern can lead to major risks in
breadbasket regions that are important for crop production. The storyline approach presented here provides insightful results
that help understand the risks and consequences of similar events in a future climate. Our results highlight that large areas of
the Northern Hemisphere will suffer from major heat stress given the same circulation at higher background warming levels,
300   which can have dangerous consequences for agriculture, ecosystems, the economy and also human health.

Code availability.   The python code for the sea ice algorithm developed in this study is currently available upon request and will be published
in a repository during the review process.

Appendix A: Additional figures

This section provides additional figures accompanying the main article.
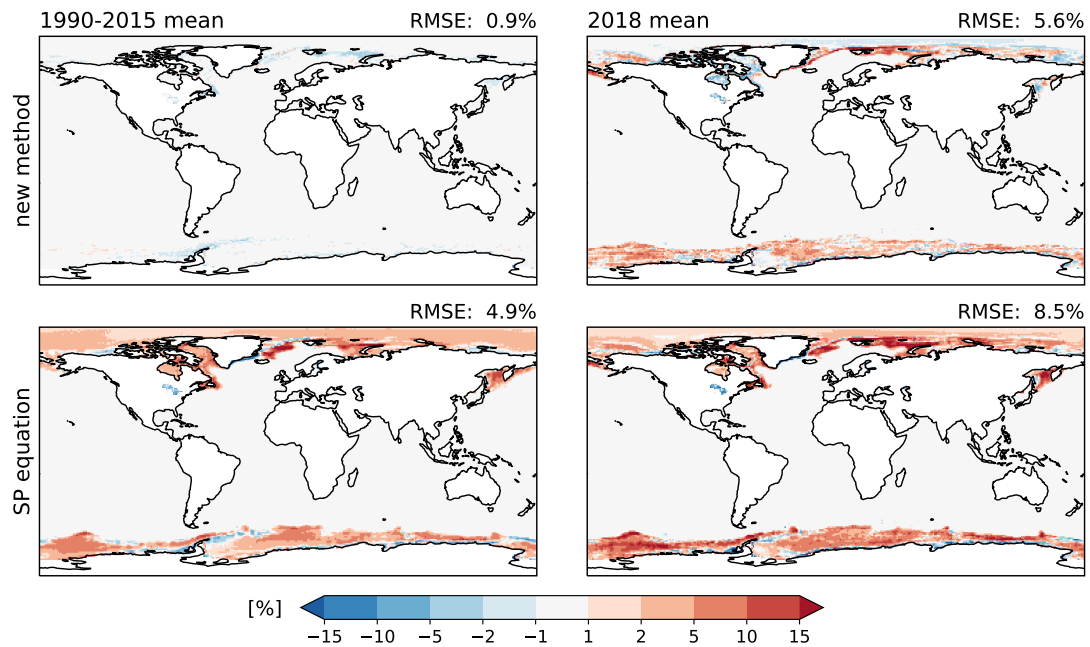
Figure A1. Evaluation of sea ice reconstruction. Bias of reconstructed historical sea ice for 1990–2015 (left) and 2018 (right) compared to NOAA OIv2 (%). The new method developed in this study (top) is compared to the SP equation. Numbers in the upper right corner indicate the RMSE for grid cells that are covered by ice in the observed or estimated fields.
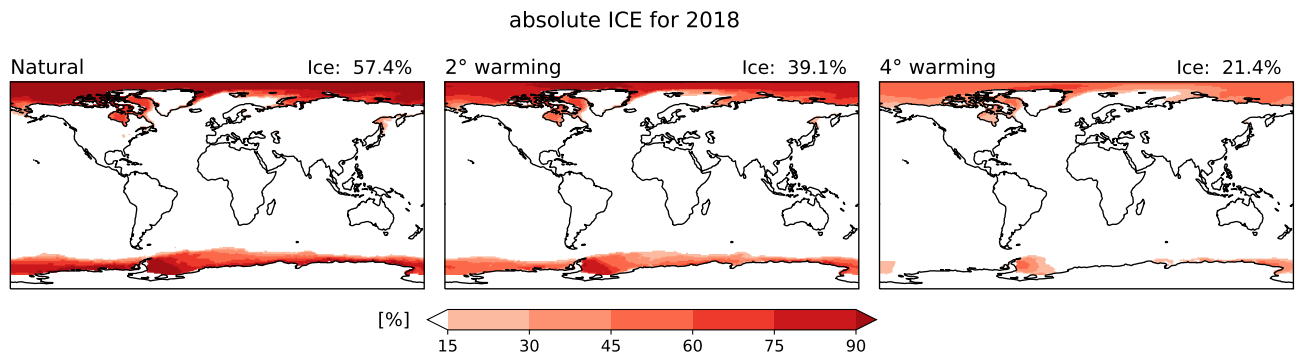
Figure A2. Absolute sea ice coverage fractions for 2018 in the natural, warming20 and warming40 simulation determined with the algorithm presented in this study. The numbers in the upper right corner indicate the yearly average sea ice coverage fraction for ice grid cells.
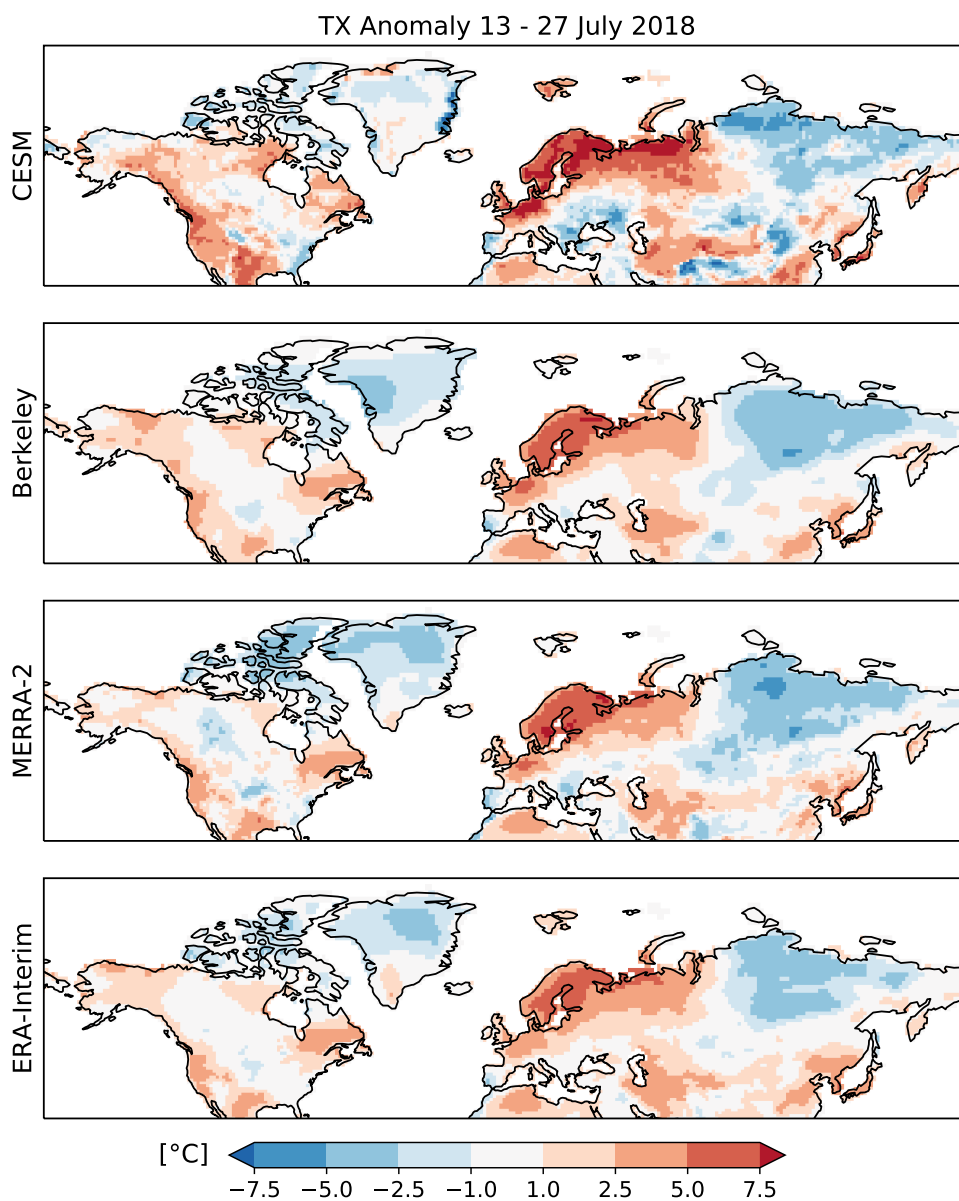
Figure A3. Anomalies of maximum daily temperature (TX) averaged over July 13 to 27 2018 with respect to the 1981–2010 climatology for the historical simulations, ERA-Interim, MERRA-2 and Berkeley.
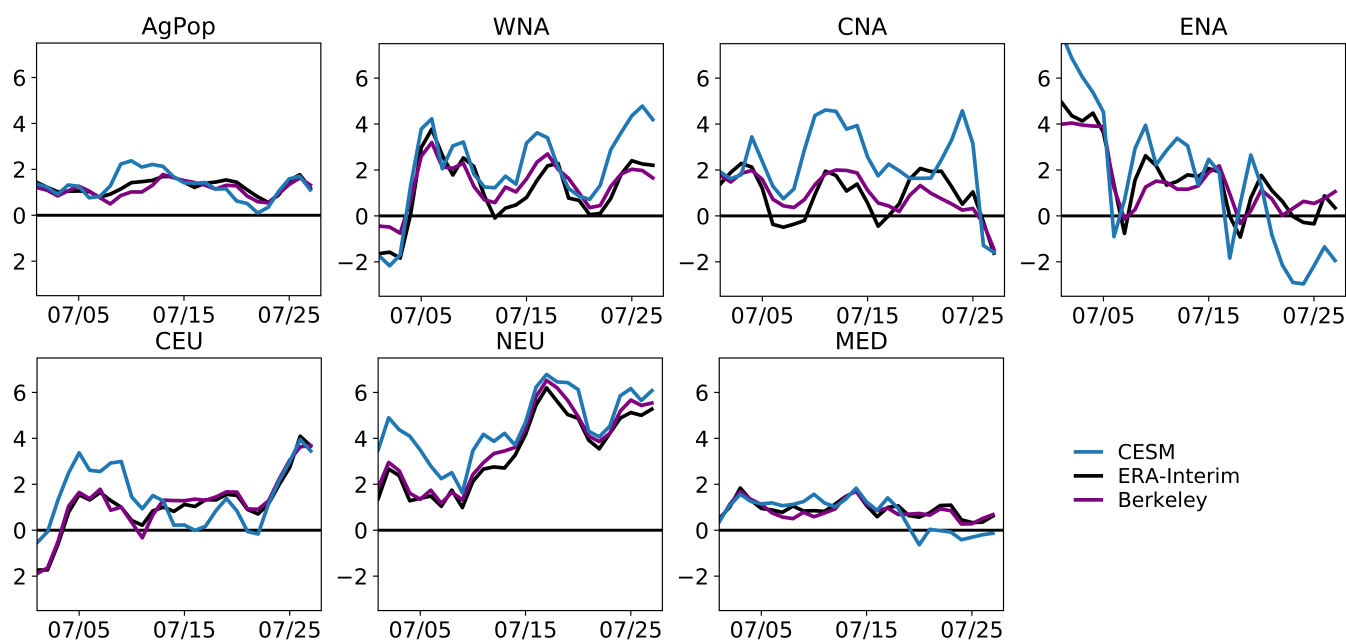
Figure A4. Time series of anomaly of maximum daily temperature for July 2018 averaged for the AgPop region and six SREX regions. Shown are the historical simulation from CESM, ERA-Interim and Berkeley. The reference climatology is 1981–2010.

305 **Appendix B: Ocean forcing files**

This section explains in detail how the ocean forcing files are prepared using model output for the historical and RCP8.5 scenario from the CMIP5 data archive.

B1   Step-by-step generation of delta SST and SST input files

Warming levels are determined using near-surface air temperature ("tas") from CMIP5. Delta SSTs are computed from sea
310   surface temperature fields ("tos").

1. For easier computation later-on and to prevent steep gradients at the continent's edges, the tos fields are grid-filled using Poisson's equation relaxation scheme, where this has not been done by the model. All data are regridded to the 1x1 degree grid used in the NOAA OIv2 (Reynolds et al., 2002) and HadISST1 (Rayner et al., 2003) observational products, which are used to prescribe sea surface temperatures and sea ice coverage in CESM.

315   2. To find the years corresponding to the warming levels we compute weighted global yearly means for the historical and RCP8.5 time period. We only include models that provide complete monthly data for both tas and tos for the historical (starting latest 1861) and the RCP8.5 time period (at least until 2099).

3. We define the pre-industrial reference period from 1861–1880 and average over this period for each model separately. We compute the warming per model by taking the difference between the yearly averages from step 2 and the pre-industrial
320   reference period. We compute a 21-year running mean over the yearly warming values and then take the multi-model mean (MMM).

4. The first year where the multi model warming equals 1.5°C, 2°C, 3°C and 4°C is chosen to compute the delta SST fields in the following and also to set the aerosols and GHG forcing from the RCP8.5 scenarios for the simulations. We get: for the current warming (2018) a value of 1.12° and the 1.5°, 2°, 3° and 4° warming levels are reached in 2028, 2042,
325   2064, 2085 respectively, for the MMM.

5. A 21-year boxcar filter (running mean over months) is applied to the monthly tos fields for the merged historical (1975–2005) + RCP8.5 time period. These ocean fields are saved together with the multi-year monthly averaged fields for the pre-industrial time period (1861–1880).

6. The MMM is computed for the monthly ocean fields. Then the delta SST for the natural scenario is computed by sub-
330   tracting the MMM pre-industrial monthly climatology from the present-day monthly fields (1979–2020). The delta SSTs for the warming scenarios are computed by subtracting the present-day monthly fields (1979–2020) from the MMM field of the year of the warming scenario under consideration, hence:

deltaSST_natural: present - pre-industrial; for *present* between 1979–2020 and *pre-industrial* averaged over 1861–1880.
335   deltaSST_warming20: 20warming - present; for *20warming* corresponding to year 2042 (with the 21-year boxcar filter

applied to it first) and *present* between 1979–2020.

Note that the delta SSTs computed this way are transient.

7. We compute the SST input for the simulations simply by subtracting the natural deltaSST field and adding the warming
340   deltaSST fields to the historical SSTs of the model. We ensure that temperature is not below $-1.8°C$.

Author contributions. KW, MH and SIS designed the experiments and discussed the results. KW developed the sea ice reconstruction method with input by MH and based on code used for HAPPI that was made available by Eunice Lo from University of Bristol. KW ran the model simulation and analysed the results. KW prepared the manuscript with contributions from all co-authors

Competing interests. The authors declare that they have no conflict of interest.

345 *Acknowledgements.* We thank Eunice Lo for sharing the HAPPI sea ice code. We acknowledge support from the European Research Council (ERC) 'DROUGHT-HEAT' project (Grant 617518) funded by the European Community's Seventh Framework Programme.

References

Cowtan, K., Hausfather, Z., Hawkins, E., Jacobs, P., Mann, M. E., Miller, S. K., Steinman, B. A., Stolpe, M. B., and Way, R. G.: Robust comparison of climate models with observations using blended land air and ocean sea surface temperatures, Geophysical Research Letters, 42, 6526–6534, https://doi.org/10.1002/2015GL064888, 2015.

Dee, D. P., Uppala, S. M., Simmons, A. J., Berrisford, P., Poli, P., Kobayashi, S., Andrae, U., Balmaseda, M. A., Balsamo, G., Bauer, P., Bechtold, P., Beljaars, A. C. M., van de Berg, L., Bidlot, J., Bormann, N., Delsol, C., Dragani, R., Fuentes, M., Geer, A. J., Haimberger, L., Healy, S. B., Hersbach, H., Hólm, E. V., Isaksen, L., Kållberg, P., Köhler, M., Matricardi, M., McNally, A. P., Monge-Sanz, B. M., Morcrette, J. J., Park, B. K., Peubey, C., de Rosnay, P., Tavolato, C., Thépaut, J. N., and Vitart, F.: The ERA-Interim reanalysis: configuration and performance of the data assimilation system, Quarterly Journal of the Royal Meteorological Society, 137, 553–597, https://doi.org/https://doi.org/10.1002/qj.828, 2011.

Dlugokencky, E.: NOAA/ESRL, www.esrl.noaa.gov/gmd/ccgg/trends_ch4/, accessed 16 October 2019, 2019.

Dlugokencky, E. and Tans, P.: NOAA/ESRL, www.esrl.noaa.gov/gmd/ccgg/trends/, accessed 16 October 2019, 2019.

Drouard, M., Kornhuber, K., and Woollings, T.: Disentangling dynamic contributions to summer 2018 anomalous weather over Europe, Geophysical Research Letters, 46, 12 537–12 546, https://doi.org/10.1029/2019GL084601, 2019.

Fischer, E. M., Seneviratne, S. I., Vidale, P. L., Lüthi, D., and Schär, C.: Soil moisture–atmosphere interactions during the 2003 European Summer Heat Wave, Journal of Climate, 20, 5081–5099, https://doi.org/https://doi.org/10.1175/JCLI4288.1, 2007.

Gelaro, R., McCarty, W., Suárez, M. J., Todling, R., Molod, A., Takacs, L., Randles, C. A., Darmenov, A., Bosilovich, M. G., Reichle, R., Wargan, K., Coy, L., Cullather, R., Draper, C., Akella, S., Buchard, V., Conaty, A., da Silva, A. M., Gu, W., Kim, G.-K., Koster, R., Lucchesi, R., Merkova, D., Nielsen, J. E., Partyka, G., Pawson, S., Putman, W., Rienecker, M., Schubert, S. D., Sienkiewicz, M., and Zhao, B.: The Modern-Era Retrospective Analysis for Research and Applications, version 2 (MERRA-2), Journal of Climate, 30, 5419–5454, https://doi.org/https://doi.org/10.1175/JCLI-D-16-0758.1, 2017.

Hazeleger, W., van den Hurk, B. J. J. M., Min, E., van Oldenborgh, G. J., Petersen, A. C., Stainforth, D. A., Vasileiadou, E., and Smith, L. A.: Tales of future weather, Nature Climate Change, 5, 107–113, https://doi.org/10.1038/nclimate2450, 2015.

Hurrell, J. W., Hack, J. J., Shea, D., Caron, J. M., and Rosinski, J.: A new sea surface temperature and sea ice boundary dataset for the Community Atmosphere Model, Journal of Climate, 21, 5145–5153, https://doi.org/https://doi.org/10.1175/2008JCLI2292.1, 2008.

Hurrell, J. W., Holland, M. M., Gent, P. R., Ghan, S., Kay, J. E., Kushner, P. J., Lamarque, J.-F., Large, W. G., Lawrence, D., Lindsay, K., Lipscomb, W. H., Long, M. C., Mahowald, N., Marsh, D. R., Neale, R. B., Rasch, P., Vavrus, S., Vertenstein, M., Bader, D., Collins, W. D., Hack, J. J., Kiehl, J., and Marshall, S.: The Community Earth System Model: A framework for collaborative research, Bulletin of the American Meteorological Society, 94, 1339–1360, https://doi.org/https://doi.org/10.1175/BAMS-D-12-00121.1, 2013.

Jones, P. W.: First- and second-order conservative remapping schemes for grids in spherical coordinates, Monthly Weather Review, 127, 2204–2210, https://doi.org/10.1175/1520-0493(1999)127<2204:FASOCR>2.0.CO;2, 1999.

Kooperman, G. J., Pritchard, M. S., Ghan, S. J., Wang, M., Somerville, R. C. J., and Russell, L. M.: Constraining the influence of natural variability to improve estimates of global aerosol indirect effects in a nudged version of the Community Atmosphere Model 5, Journal of Geophysical Research: Atmospheres, 117, https://doi.org/https://doi.org/10.1029/2012JD018588, d23204, 2012.

Kornhuber, K., Coumou, D., Vogel, E., Lesk, C., Donges, J. F., Lehmann, J., and Horton, R. M.: Amplified Rossby waves enhance risk of concurrent heatwaves in major breadbasket regions, Nature Climate Change, https://doi.org/10.1038/s41558-019-0637-z, https://doi.org/10.1038/s41558-019-0637-z, 2019a.

Kornhuber, K., Osprey, S., Coumou, D., Petri, S., Petoukhov, V., Rahmstorf, S., and Gray, L.: Extreme weather events in early summer 2018
385   connected by a recurrent hemispheric wave-7 pattern, Environmental Research Letters, 14, https://doi.org/10.1088/1748-9326/ab13bf,
       2019b.

Lawrence, D. M., Oleson, K. W., Flanner, M. G., Thornton, P. E., Swenson, S. C., Lawrence, P. J., Zeng, X., Yang, Z.-L., Levis, S., Sakaguchi,
       K., Bonan, G. B., and Slater, A. G.: Parameterization improvements and functional and structural advances in version 4 of the Community
       Land Model, Journal of Advances in Modeling Earth Systems, 3, https://doi.org/https://doi.org/10.1029/2011MS00045, 2011.

390   Matthes, K., Funke, B., Andersson, M. E., Barnard, L., Beer, J., Charbonneau, P., Clilverd, M. A., Dudok de Wit, T., Haberreiter, M., Hendry,
       A., Jackman, C. H., Kretzschmar, M., Kruschke, T., Kunze, M., Langematz, U., Marsh, D. R., Maycock, A. C., Misios, S., Rodger, C. J.,
       Scaife, A. A., Seppälä, A., Shangguan, M., Sinnhuber, M., Tourpali, K., Usoskin, I., van de Kamp, M., Verronen, P. T., and Versick, S.:
       Solar forcing for CMIP6 (v3.2), Geoscientific Model Development, 10, 2247–2302, https://doi.org/https://doi.org/10.5194/gmd-10-2247-
       2017, 2017.

395   Mitchell, D., AchutaRao, K., Allen, M., Bethke, I., Beyerle, U., Ciavarella, A., Forster, P. M., Fuglestvedt, J., Gillett, N., Haustein, K., Ingram,
       W., Iversen, T., Kharin, V., Klingaman, N., Massey, N., Fischer, E., Schleussner, C.-F., Scinocca, J., Seland, Ø., Shiogama, H., Shuckburgh,
       E., Sparrow, S., Stone, D., Uhe, P., Wallom, D., Wehner, M., and Zaaboul, R.: Half a degree additional warming, prognosis and projected
       impacts (HAPPI): Background and experimental design, Geoscientific Model Development, 10, 571–583, https://doi.org/10.5194/gmd-
       10-571-2017, 2017.

400   Neale, R. B., Chen, C.-C., Gettelman, A., Lauritzen, P. H., Park, S., Williamson, D. L., Conley, A. J., Garcia, R., Kinnison, D., Lamarque,
       J.-F., Marsh, D., Mills, M., Smith, A. K., Tilmes, S., Vitt, F., Morrison, H., Cameron-Smith, P., Collins, W. D., Iacono, M. J., Easter, R. C.,
       Ghan, S. J., Liu, X., Rasch, P. J., and Taylor, M. A.: Description of the NCAR Community Atmosphere Model (CAM 5.0), Technical
       report, National Center for Atmospheric Research. Boulder, Colorado, 2012.

NOAA: State of the climate: Global climate report for July 2018, National Centers for Environmental Information, https://www.ncdc.noaa.
405   gov/sotc/global/201807, 2018.

NOAA Earth System Research Laboratory: Combined nitrous oxide data from the NOAA/ESRL Global Monitoring Division, ftp://ftp.cmdl.
       noaa.gov/hats/n2o/combined/HATS_global_N2O.txt, accessed 16 October 2019, 2019.

Oleson, K. W., Lawrence, D. M., Bonan, G. B., Flanner, M. G., Kluzek, E., Lawrence, P. J., Levis, S., Swenson, S. C., Thornton, P. E., Dai,
       A., Decker, M., Dickinson, R., Feddema, J., Heald, C. L., Hoffman, F., Lamarque, J.-F., Mahowald, N., Niu, G.-Y., Qian, T., Randerson,
410   J., Running, S., Sakaguchi, K., Slater, A., Stöckli, R., Wang, A., Yang, Z.-L., Zeng, X., and Zeng, X.: Technical description of version 4.0
       of the Community Land Model (CLM), Technical report, National Center for Atmospheric Research. Boulder, Colorado, 2010.

Rayner, N. A., Parker, D. E., Horton, E. B., Folland, C. K., Alexander, L. V., Rowell, D. P., Kent, E. C., and Kaplan, A.: Global analyses
       of sea surface temperature, sea ice, and night marine air temperature since the late nineteenth century, Journal of Geophysical Research:
       Atmospheres, 108, https://doi.org/10.1029/2002JD002670, 2003.

415   Reynolds, R. W., Rayner, N. A., Smith, T. M., Stokes, D. C., and Wang, W.: An improved in situ and satellite SST analysis for climate,
       Journal of Climate, 15, 1609–1625, https://doi.org/10.1175/1520-0442(2002)015<1609:AIISAS>2.0.CO;2, 2002.

Richardson, M., Cowtan, K., Hawkins, E., and Stolpe, M. B.: Reconciled climate response estimates from climate models and the energy
       budget of Earth, Nature Climate Change, 6, 931–935, https://doi.org/10.1038/nclimate3066, 2016.

Rohde, R., Muller, R. A., Jacobsen, R., Muller, E., Perlmutter, S., Rosenfeld, A., Wurtele, J., Groom, D., and Wickham, C.: A
420   new estimate of average Earth surface land temperature spanning 1743 to 2011, Geoinformatics & Geostatistics: An Overview, 1,
       https://doi.org/https://doi.org/10.4172/2327-4581.1000101, 2013a.

Rohde, R., Muller, R. A., Jacobsen, R., Perlmutter, S., Rosenfeld, A., Wurtele, J., Curry, J., Wickham, C., and Mosher, S.: Berkeley Earth temperature averaging process, Geoinformatics & Geostatistics: An Overview, 1, https://doi.org/https://doi.org/10.4172/2327-4581.1000103, 2013b.

425 Seneviratne, S. I., Luthi, D., Litschi, M., and Schar, C.: Land-atmosphere coupling and climate change in Europe, Nature, 443, 205–209, https://doi.org/https://doi.org/10.1038/nature05095, 2006.

Seneviratne, S. I., Corti, T., Davin, E. L., Hirschi, M., Jaeger, E. B., Lehner, I., Orlowsky, B., and Teuling, A. J.: Investigating soil moisture–climate interactions in a changing climate: A review, Earth-Science Reviews, 99, 125–161, https://doi.org/https://doi.org/10.1016/j.earscirev.2010.02.004, 2010.

430 Seneviratne, S. I., Nicholls, N., Easterling, D., Goodess, C. M., Kanae, S., Kossin, J., Luo, Y., Marengo, J., Innes, K. M., Rahimi, M., Reichstein, M., Sorteberg, A., Vera, C., Zhang, X., Rusticucci, M., Semenov, V., Alexander, L. V., Allen, S., Benito, G., Cavazos, T., Clague, J., Conway, D., Della-Marta, P. M., Gerber, M., Gong, S., Goswami, B. N., Hemer, M., Huggel, C., den Hurk, B. V., Kharin, V. V., Kitoh, A., Tank, A. M. G. K., Li, G., Mason, S., Guire, W. M., Oldenborgh, G. J. V., Orlowsky, B., Smith, S., Thiaw, W., Velegrakis, A., Yiou, P., Zhang, T., Zhou, T., and Zwiers, F. W.: Changes in climate extremes and their impacts on the natural physical environment, in:

435 Managing the Risks of Extreme Events and Disasters to Advance Climate Change Adaptation, pp. 109–230, edited by C. B. Field et al., Cambridge University Press, Cambridge, https://doi.org/https://doi.org/10.1017/CBO9781139177245.006, 2012.

Seneviratne, S. I., Phipps, S. J., Pitman, A. J., Hirsch, A. L., Davin, E. L., Donat, M. G., Hirschi, M., Lenton, A., Wilhelm, M., and Kravitz, B.: Land radiative management as contributor to regional-scale climate adaptation and mitigation, Nature Geoscience, 11, 88–96, https://doi.org/10.1038/s41561-017-0057-5, 2018.

440 Shepherd, T. G., Boyd, E., Calel, R. A., Chapman, S. C., Dessai, S., Dima-West, I. M., Fowler, H. J., James, R., Maraun, D., Martius, O., Senior, C. A., Sobel, A. H., Stainforth, D. A., Tett, S. F. B., Trenberth, K. E., van den Hurk, B. J. J. M., Watkins, N. W., Wilby, R. L., and Zenghelis, D. A.: Storylines: An alternative approach to representing uncertainty in physical aspects of climate change, Climatic Change, 151, 555–571, https://doi.org/10.1007/s10584-018-2317-9, 2018.

Stone, D. A., Christidis, N., Folland, C., Perkins-Kirkpatrick, S., Perlwitz, J., Shiogama, H., Wehner, M. F., Wolski, P., Cho-
445 lia, S., Krishnan, H., Murray, D., Angélil, O., Beyerle, U., Ciavarella, A., Dittus, A., Quan, X.-W., and Tadross, M.: Experiment design of the International CLIVAR C20C+ Detection and Attribution project, Weather and Climate Extremes, 24, https://doi.org/https://doi.org/10.1016/j.wace.2019.100206, 2019.

Taylor, K. E., Stouffer, R. J., and Meehl, G. A.: An overview of CMIP5 and the experiment design, Bulletin of the American Meteorological Society, 93, 485–498, https://doi.org/https://doi.org/10.1175/BAMS-D-11-00094.1, 2012.

450 Toreti, A., Belward, A., Perez-Dominguez, I., Naumann, G., Luterbacher, J., Cronie, O., Seguini, L., Manfron, G., Lopez-Lozano, R., Baruth, B., van den Berg, M., Dentener, F., Ceglar, A., Chatzopoulos, T., and Zampieri, M.: The exceptional 2018 European water seesaw calls for action on adaptation, Earth's Future, 7, 652–663, https://doi.org/10.1029/2019EF001170, 2019.

van Vuuren, D. P., Edmonds, J., Kainuma, M., Riahi, K., Thomson, A., Hibbard, K., Hurtt, G. C., Kram, T., Krey, V., Lamarque, J.-F., Masui, T., Meinshausen, M., Nakicenovic, N., Smith, S. J., and Rose, S. K.: The representative concentration pathways: An overview, Climatic
455 Change, 109, 5, https://doi.org/https://doi.org/10.1007/s10584-011-0148-z, 2011.

Vogel, M. M., Zscheischler, J., Wartenburger, R., Dee, D., and Seneviratne, S. I.: Concurrent 2018 hot extremes across Northern Hemisphere due to human-induced climate change, Earth's Future, 7, 692–703, https://doi.org/10.1029/2019EF001189, 2019.

Wehrli, K., Guillod, B. P., Hauser, M., Leclair, M., and Seneviratne, S. I.: Assessing the dynamic versus thermodynamic origin of climate model biases, Geophysical Research Letters, 45, 8471–8479, https://doi.org/https://doi.org/10.1029/2018GL079220, 2018.

460 Wehrli, K., Guillod, B. P., Hauser, M., Leclair, M., and Seneviratne, S. I.: Identifying key driving processes of major recent heat waves, Journal of Geophysical Research: Atmospheres, 124, 11 746–11 765, https://doi.org/10.1029/2019JD030635, 2019.

Zhang, K., Wan, H., Liu, X., Ghan, S. J., Kooperman, G. J., Ma, P.-L., Rasch, P. J., Neubauer, D., and Lohmann, U.: Technical note: On the use of nudging for aerosol–climate model intercomparison studies, Atmospheric Chemistry and Physics, 14, 8631–8645, https://doi.org/https://doi.org/10.5194/acp-14-8631-2014, 2014.